



## O<sub>2</sub> plasma activation of dendrimer-derived Pt/ $\gamma$ -Al<sub>2</sub>O<sub>3</sub> catalysts

Zahra Nazarpour<sup>a</sup>, Shuguo Ma<sup>a</sup>, Paul T. Fanson<sup>b</sup>, Oleg S. Alexeev<sup>a,\*</sup>, Michael D. Amiridis<sup>a,\*</sup>

<sup>a</sup> Department of Chemical Engineering, University of South Carolina, Columbia, SC 29208, USA

<sup>b</sup> Materials Research Department, Toyota Motor Engineering & Manufacturing North America, Inc., Ann Arbor, MI 48105, USA

### ARTICLE INFO

#### Article history:

Received 20 November 2011

Revised 22 February 2012

Accepted 23 February 2012

Available online 13 April 2012

#### Keywords:

Platinum nanoparticles

PAMAM dendrimers

O<sub>2</sub> plasma

CO oxidation

Ethane hydrogenolysis

### ABSTRACT

Platinum particles, approximately 1.6 nm in size, were formed on  $\gamma$ -Al<sub>2</sub>O<sub>3</sub> following impregnation with a Pt<sub>40</sub>-dendrimer precursor solution. These Pt particles are not catalytically active, since they are covered by the dendrimer component. Treatment in O<sub>2</sub> plasma at room temperature removes the dendrimer without affecting metal dispersion. Subsequent treatment in H<sub>2</sub> at 300 °C leads to partial aggregation of Pt, although the degree of such aggregation is relatively small, as the average size of the Pt particles remains approximately 2 nm. In contrast, when a high temperature oxidation/reduction treatment is used to activate the Pt<sub>40</sub>-dendrimer/ $\gamma$ -Al<sub>2</sub>O<sub>3</sub> material, sintering of Pt is observed and the average Pt particle size increases to approximately 4 nm. Kinetic data obtained with Pt/ $\gamma$ -Al<sub>2</sub>O<sub>3</sub> catalysts activated under both protocols for the structure-insensitive CO oxidation and the structure-sensitive ethane hydrogenolysis reactions underline the differences in the sizes of the Pt particles in these materials, consistent with previous literature reports.

© 2012 Elsevier Inc. All rights reserved.

### 1. Introduction

It has been suggested in the literature that colloidal nanoparticles formed in solution can be used as precursors for the preparation of heterogeneous catalysts [1–5]. Since at least in principle, the size, structure, and composition of such nanoparticles can be controlled precisely in solution, this preparation concept can open up a new avenue for the controlled synthesis of supported metal catalysts. The preparation of colloidal metal nanoparticles requires the reduction of transition metal ions in an aqueous or organic medium. This step is typically performed in the presence of surfactants, acting as protective agents, to preserve the colloidal state of the metal particles formed [1–5]. Several chemical compounds, such as poly(vinylpyrrolidone) (PVP), poly(vinylalcohol) (PVA), polyoxoanions, and various types of dendrimers containing amide and/or amine groups have been used in this role. Literature reports further demonstrate that colloidal nanoparticles can be successfully deposited onto various supports [1–4,6–8]. The resulting catalysts typically exhibit narrower particle size distributions than those observed with conventionally prepared materials of similar composition on the same supports.

Potential limitations in the application of this preparation method include the incomplete reduction of the metal precursor and the need for the removal of the polymeric protective agent

during final catalyst activation [7,8]. For example, in the case of dendrimer-stabilized nanoparticles, thermal treatments have been used to remove the dendrimer component and such treatments lead to sintering of the metal nanoparticles. Along these lines, extended X-ray absorption fine structure spectroscopy (EXAFS) data reported for dendrimer-derived Pt/ $\gamma$ -Al<sub>2</sub>O<sub>3</sub> catalysts indicate that the Pt–Pt first-shell coordination number increases from 5.6 to 11.2 after high temperature oxidation/reduction treatments are used to remove the dendrimer and activate the Pt [7]. Similarly, significant sintering of Ru and Rh was observed during thermal pretreatment of dendrimer-derived Ru/ $\gamma$ -Al<sub>2</sub>O<sub>3</sub> and Rh/SBA-15 materials [9,10]. In contrast, the synthesis of highly dispersed and nearly uniform Rh nanoparticles with sub-nanometer dimensions was reported in the case of dendrimer-derived Rh/ZrO<sub>2</sub> [8]. These contrasting examples for different combinations of metals and supports indicate that in each specific case, the degree of the metal sintering depends on the nature of these components. While some optimization of the thermal treatment conditions may limit sintering in a few of these cases, it does not appear that sintering can be completely avoided. It is therefore, critical to examine alternative solutions and explore treatments capable of removing the dendrimer component without altering the architecture of the metal nanoparticles, especially for cases in which the resulting catalyst is intended for use in applications under mild temperature conditions.

In this respect, plasma treatments could provide a viable solution. In the past, low temperature plasma treatments have been used frequently to clean surfaces of solid materials from organic contaminations [11,12]. More recent examples also demonstrate

\* Corresponding authors. Fax: +1 803 7778265 (O.S. Alexeev), fax: +1 803 7779502 (M.D. Amiridis).

E-mail addresses: [alexeev@cec.sc.edu](mailto:alexeev@cec.sc.edu) (O.S. Alexeev), [amiridis@cec.sc.edu](mailto:amiridis@cec.sc.edu) (M.D. Amiridis).

the use of plasma for the preparation of supported metal catalysts [13–16]. In these examples, the plasma treatment not only leads to the decomposition of inorganic metal salts or the removal of organic ligands from the metal precursors used but is also responsible for the reduction of the corresponding metal cations and the subsequent formation of metal particles. We have also demonstrated that an O<sub>2</sub> plasma treatment at room temperature can be used successfully to decompose and remove fourth-generation hydroxyl-terminated (G4OH) poly(amidoamine) (PAMAM) dendrimer molecules from a  $\gamma$ -Al<sub>2</sub>O<sub>3</sub> surface [17].

In this paper, we examine the effect of the O<sub>2</sub> plasma treatment on the properties of the Pt species present in dendrimer-derived Pt/ $\gamma$ -Al<sub>2</sub>O<sub>3</sub> catalysts. This material was chosen because it was well characterized previously during all preparation steps and exhibited the highest degree of metal sintering among all combinations of metals and supports examined during the thermal dendrimer removal process. Scanning transmission electron microscopy (STEM), X-ray photoelectron spectroscopy (XPS), Fourier transform infrared spectroscopy (FTIR), and EXAFS measurements were used to characterize this material after exposure to O<sub>2</sub> plasma. Catalytic data were also collected for the oxidation of CO and the hydrogenolysis of ethane, demonstrating the effect of activation protocols on the catalytic performance.

## 2. Experimental methods

### 2.1. Reagents and materials

Fourth-generation hydroxyl-terminated (G4OH) poly(amidoamine) (PAMAM) dendrimer was purchased as a 10% solution in methanol (Dendritech Inc.). Prior to use, the methanol was removed under N<sub>2</sub> flow at room temperature, and a 0.17 mM aqueous solution of the G4OH PAMAM dendrimer was prepared and stocked. H<sub>2</sub>PtCl<sub>6</sub>·6H<sub>2</sub>O (99.5% purity, Alfa Aesar) was used as supplied. Water purified to 18 M $\Omega$  cm<sup>−1</sup> (Milli-Q grade) was used to prepare all aqueous solutions. The  $\gamma$ -Al<sub>2</sub>O<sub>3</sub> support (Catalox SBA-200, Sasol), with a BET surface area of 190 m<sup>2</sup>/g and a pore volume of 0.45 ml/g, was calcined in air at 500 °C for 4 h prior to use. Ultra high purity grade H<sub>2</sub>, N<sub>2</sub>, and He (Airgas National Welders) were additionally purified from traces of moisture and oxygen by passage through appropriate traps (Agilent, models GMT-2GCHP and OT-3, respectively). Other gases (i.e., 10% O<sub>2</sub>/He and 1000 ppm CO/500 ppm O<sub>2</sub>/He mixtures; Airgas National Welders) were used as received.

### 2.2. Preparation of Pt<sub>40</sub>-G4OH/ $\gamma$ -Al<sub>2</sub>O<sub>3</sub>

The dendrimer-derived Pt<sub>40</sub>-G4OH/ $\gamma$ -Al<sub>2</sub>O<sub>3</sub> sample was prepared as reported previously [7]. In brief, aqueous solutions of the H<sub>2</sub>PtCl<sub>6</sub>·6H<sub>2</sub>O precursor and the G4OH PAMAM dendrimer were mixed in appropriate amounts to obtain a molar ratio of Pt to dendrimer equal to 40. The mixture was stirred at room temperature under nitrogen flow for 5 days to complete the complexation process, and the solution was dialyzed to remove impurities using a benzoylated cellulose dialysis sack with a molecular weight cut-off of 2000. (Pt<sup>n+</sup>)<sub>40</sub>-G4OH nanocomposites thus formed in solution were further treated with H<sub>2</sub> at room temperature for 2 h. EXAFS data reported elsewhere [7] suggest that such a treatment leads to the formation of very small Pt clusters, most likely Pt dimers. The supported Pt<sub>40</sub>-G4OH/ $\gamma$ -Al<sub>2</sub>O<sub>3</sub> sample was prepared by slurring of the H<sub>2</sub>-treated (Pt<sup>n+</sup>)<sub>40</sub>-G4OH solution with the  $\gamma$ -Al<sub>2</sub>O<sub>3</sub> support in amounts chosen to yield samples containing 0.5 wt.% Pt. The excess water was removed by slow evaporation at room temperature. The resulting solid samples were finally treated in O<sub>2</sub> plasma at room temperature for 1 h to remove the dendrimer com-

ponent. In some cases, O<sub>2</sub> plasma-treated samples were treated subsequently in H<sub>2</sub> at 300 °C for 1 h. The Pt weight loading was verified by atomic absorption spectroscopy.

### 2.3. O<sub>2</sub> plasma treatment

A benchtop PE-100 apparatus (PlasmaEtch) equipped with a vacuum chamber and a NESLAB RTE7 refrigerated bath was used for O<sub>2</sub> plasma treatments. This equipment was operated at room temperature, a residual pressure of 0.3 Torr, a radio frequency power of 250 W, and a total O<sub>2</sub> flow of 25 ml/min. Powder samples were treated in the form of a thin layer placed on a Petri dish.

### 2.4. Infrared spectroscopy

A Nicolet Nexus 470 spectrometer equipped with a MCT-B detector cooled by liquid nitrogen was used to record FTIR spectra with a resolution of 2 cm<sup>−1</sup>, accumulating 64 scans per spectrum. Samples were pressed into self-supported wafers with a density of approximately 30 mg/cm<sup>2</sup> and mounted in a home-made FTIR cell connected to a gas distribution manifold. Prior to each experiment, the cell was purged with He at 25 °C for approximately 2 h and initial spectra were collected under the flow of He. Any additional thermal treatments required were performed in situ in the cell.

### 2.5. XPS measurements

A Kratos AXIS Ultra DLD X-ray photoelectron spectrometer equipped with a monochromatic Al K $\alpha$  source operated at 15 keV and 150 W was used for XPS measurements. The pass energy was fixed at 40 eV for the detailed scans. A charge neutralizer was used to compensate for the surface charging during the photoemission process. All powder samples were pressed into a cup of a Mo stub and mounted in a Kratos catalysis cell attached to the XPS system that allows for various treatments under high temperature and pressure conditions. Treated samples were then transferred without air exposure into the UHV chamber for the XPS analysis. Since the Al 2p and Pt 4f signals overlap, the Al 2s signal with a binding energy of 119.2 eV was used as an internal reference for calibration of the Pt 4d lines in all samples examined. All binding energies reported in this work were measured with a precision of  $\pm 0.2$  eV.

XPS data were analyzed by nonlinear curve fitting using the PeakFit 4.12 software. In all cases, a linear-type background was subtracted from the spectra and a curve fit was performed with the minimum number of Voigt G/L-type peaks that provides a good fit. In each case, FWHM values were fixed between 4.0 and 4.8 eV, consistent with previous literature reports [18], and the fitting routine was completed when the coefficient of determination ( $R^2$ ) value was 0.98 or higher. The difference between binding energies of the Pt 4d<sub>5/2</sub> and 4d<sub>3/2</sub> doublet was found to be approximately 17.0 eV in all spectra, consistent with previous literature reports [18–21].

### 2.6. STEM measurements

Scanning transmission electron microscopy (STEM) images were recorded using a JEOL-2100F instrument equipped with a CEOS aberration corrector on the illuminating optics. The instrument provides a spatial resolution of 1 Å and operates at 200 keV. A small quantity of each sample was placed on a carbon-coated 200-mesh copper grid, and the sample was imaged without any further treatment. Average particle sizes were calculated as  $D = \frac{\sum n_i d_i^3}{\sum n_i d_i^2}$  (where  $n_i$  is the number of particles with the

$d_i$  diameter), after measuring at least 200 particles from different images for each sample.

### 2.7. Chemisorption measurements

A ChemBET-3000 pulse chemisorption analyzer (Quanta-chrome) was used for chemisorption measurements. In a typical experiment, the sample (0.3 g) was loaded into a fixed-bed quartz reactor and reduced in situ with  $H_2$  at 300 °C for 1 h. When the reduction step was completed, the sample was purged with  $N_2$  at 300 °C for 1 h and cooled down to room temperature under the flow of  $N_2$ . A known volume of  $H_2$  or  $O_2$  was then pulsed through the sample in 4 min intervals, and the amount of each gas chemisorbed by the sample was measured at room temperature and atmospheric pressure. The adsorption stoichiometry (the number of Pt atoms per hydrogen or oxygen molecule) was assumed to be 2, and the metal dispersion values obtained were used to calculate average sizes of Pt particles based on the following equation:  $D_{Pt} \text{ (nm)} = \frac{1.132}{P_{t_s}/P_{t_t}}$  (where  $P_{t_s}/P_{t_t}$  is the fraction of Pt atoms exposed). A spherical shape was assumed in these calculations for the Pt particles.

### 2.8. XAS measurements

X-ray absorption spectroscopy (XAS) measurements were performed at X-ray beamline 10–2 of the Stanford Synchrotron Radiation Laboratory (SSRL), Stanford Linear Accelerator Center, Menlo Park, CA. The storage ring electron energy was 3 GeV and the ring current was 80–100 mA. Data were collected at liquid nitrogen temperature with a Si (220) double-crystal monochromator that was detuned by 40% to minimize the effects of higher harmonics in the X-ray beam. The data used for each sample were the averages of four scans.

The  $Pt_{40}\text{-G4OH}/\gamma\text{-Al}_2\text{O}_3$  samples were loaded as wafers into an in situ XAS cell [22] connected to a gas distribution system allowing for the treatment for the samples with various gases. After a desired treatment was completed, the XAS cell was evacuated at room temperature to  $10^{-5}$  Torr, cooled to nearly liquid nitrogen temperature, and aligned in the X-ray beam. The XAS data were recorded in the transmission mode with an appropriate amount of sample to give an absorbance of approximately 2.5 at the Pt  $L_3$  (11,564 eV) edge.

#### 2.8.1. XAS data analysis

The XDAP software developed by XAFS Services International was used for the analysis of the data [23]. The methods used to extract the EXAFS function from the raw data were essentially the same as reported elsewhere [24]. The pre-edge was subtracted using a modified Victoreen curve, and the background was removed employing cubic spline routines with a continuously adjustable smooth parameter. Normalization was performed by dividing the data by the height of the absorption edge at 50 eV.

The EXAFS data were further analyzed in  $r$ -space using the XDAP data analysis code and the multiple shell fitting routine with the application of  $k^1$  and  $k^3$  weighting in the Fourier transformations [24]. The difference file technique was applied together with phase- and amplitude-corrected Fourier transforms to resolve different contributions in the EXAFS spectra as reported previously [25,26]. Experimentally determined reference files obtained from EXAFS data for materials of known structure were used in the analysis. The Pt–Pt and Pt–O(N) interactions were analyzed with phase shifts and backscattering amplitudes obtained from EXAFS data characterizing platinum foil and  $Na_2Pt(OH)_6$ , respectively, and no attempts were made to distinguish between oxygen and nitrogen backscatterers. The Pt–C contributions were analyzed with phase shifts and backscattering amplitudes obtained from EXAFS data

characterizing crystalline  $Ir_4(CO)_{12}$ , which has only terminal CO ligands. The transferability of the phase shifts and backscattering amplitudes characterizing platinum and iridium, which are near neighbors in the Periodic table, has been justified both theoretically and experimentally [27,28]. The crystallographic coordination parameters for all reference compounds, the weighing of the Fourier transform, and the ranges in  $k$  and  $r$ -space used to extract the reference function from EXAFS data have been reported previously [29].

To simplify the data analysis in this work, the following specific procedures were applied. The raw EXAFS data obtained for each sample were Fourier transformed with a  $k^3$  weighting over the  $2.68 < k < 16.10 \text{ \AA}^{-1}$  range (where  $k$  is the wave vector) with no phase correction. The Fourier-transformed data were then inverse transformed in the  $1.00 < r < 3.40 \text{ \AA}$  range (where  $r$  is the distance from the absorbing Pt atom) to isolate the first-shell contributions from higher shells and the low-frequency noise. The data at the Pt  $L_3$  edge were analyzed with a maximum of 16 free parameters over the ranges of  $3.50 < k < 15.00 \text{ \AA}^{-1}$  and  $1.00 < r < 3.40 \text{ \AA}$ . The statistically justified number of free parameters,  $n$ , was found to be 18, as estimated on the basis of the Nyquist theorem [30,31]:  $n = (2\Delta k\Delta r/\pi) + 1$ , where  $\Delta k$  and  $\Delta r$  are the  $k$  and  $r$  ranges used in the data fitting, respectively.

### 2.9. Catalytic measurements

The oxidation of CO was performed in a quartz single-pass fixed-bed reactor at atmospheric pressure in the temperature range of 70–370 °C. The temperature inside the reactor was monitored by a thermocouple extended into the catalyst bed. Samples in the powder form (0.077 g) were diluted 90 times by weight with quartz particles (60–80 mesh) to maintain the catalyst bed isothermal. The total volumetric flow rate of the feed (i.e., 1000 ppm CO/500 ppm  $O_2$ /He) was held at 128 ml/min (1 atm, 25 °C), yielding a corresponding gas hourly space velocity (GHSV) of approximately 100,000 ml/g<sub>cat</sub> h. The reaction feed and products were analyzed with an online single beam NDIR CO (Ultramat 23, Siemens) analyzer and a GC (HP-5890) equipped with a 60/80 Carboxen 1000 column and a TCD detector. All light-off curves include data points taken after approximately 2 h on stream when steady state is reached. The TOF values were calculated at 140 °C where the CO conversion was below 10% for all samples examined.

The same experimental setup was used for the ethane hydrogenolysis measurements. In this case, flow rates of  $H_2$ ,  $C_2H_6$ , and He were controlled by mass flow controllers to obtain a feed consisting of 32.5%  $H_2$ , 6.3%  $C_2H_6$ , and 61.2% He. The total volumetric flow rate of the feed was held at 60 ml/min (1 atm, 25 °C), and the catalyst (0.056 g) was diluted 20 times by weight with quartz particles. The corresponding gas hourly space velocity (GHSV) in this case is approximately 64,000 ml/g<sub>cat</sub> h. Prior to kinetic measurements, each sample was treated in  $H_2$  at 300 °C for 1 h, purged with He at 300 °C for 30 min, heated to the desired reaction temperature under the flow of He, and then exposed to the reaction mixture. The reaction was conducted in the 325–345 °C range under differential conditions (i.e., ethane conversions below 5%). All samples exhibited deactivation, which was in the 10–33% range after 2 h on stream. Catalytic data reported herein correspond to initial rates (i.e., after approximately 5 min on stream).

## 3. Results and discussion

### 3.1. Freshly prepared $Pt_{40}\text{-G4OH}/\gamma\text{-Al}_2\text{O}_3$

The FTIR spectrum of a freshly prepared  $Pt_{40}\text{-G4OH}/\gamma\text{-Al}_2\text{O}_3$  sample is shown in Fig. 1 (spectrum 1). This spectrum is nearly

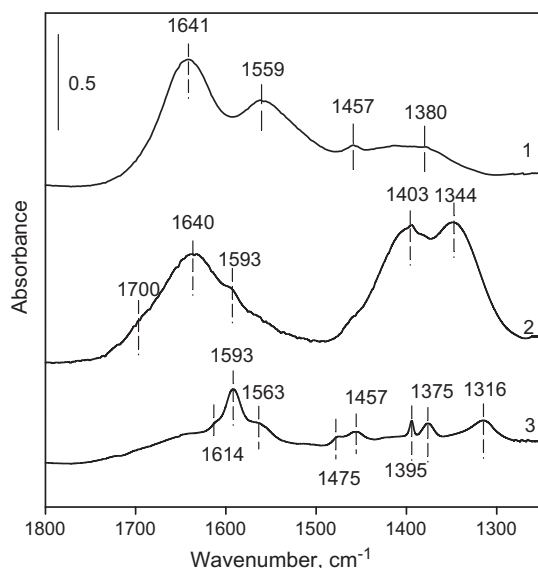


**Fig. 1.** FTIR spectra of a Pt<sub>40</sub>-G4OH/ $\gamma$ -Al<sub>2</sub>O<sub>3</sub> sample: (1) freshly prepared; (2) following treatment in O<sub>2</sub> plasma at room temperature for 1 h; (3) subsequent reduction in H<sub>2</sub> at 300 °C for 1 h.

identical to those reported previously for a G4OH PAMAM dendrimer film and a non-Pt containing G4OH/ $\gamma$ -Al<sub>2</sub>O<sub>3</sub> sample [17]. Bands observed at 1641, 1559, 1457, and 1380 cm<sup>-1</sup> have been assigned to amide I, amide II,  $\delta_{\text{CH}_2}$ , and amide III vibrations of the dendrimer species, respectively [17]. Since the Pt<sub>40</sub>-G4OH/ $\gamma$ -Al<sub>2</sub>O<sub>3</sub> sample was prepared by wet impregnation, deformation vibrations of water molecules remaining in the sample are also expected to contribute to the band at 1641 cm<sup>-1</sup> [32].

Table 1 provides a detail comparison of selected infrared bands characterizing the G4OH PAMAM dendrimer before and after impregnation on  $\gamma$ -Al<sub>2</sub>O<sub>3</sub> as well as after the dendrimer was loaded with Pt and subsequently deposited on  $\gamma$ -Al<sub>2</sub>O<sub>3</sub>. The data of Table 1 clearly show that the amide I, amide II, and  $\delta_{\text{CH}_2}$  vibrations remain unchanged in all three samples, suggesting that these vibrations are insensitive to the coordination environment. In contrast, the amide III vibration shifted to higher frequencies (by 9 cm<sup>-1</sup>) when the dendrimer was deposited on  $\gamma$ -Al<sub>2</sub>O<sub>3</sub>, and this shift further increased (i.e., 18 cm<sup>-1</sup>) when Pt was present in the sample (Table 1). Since the amide III band is primarily associated with bending and stretching vibrations involving nitrogen atoms of the amide groups [33], these results suggest that the nitrogen atoms of the amide groups interact to some degree with both the support and the Pt atoms present. Similar changes in the position of the amide III band were reported previously for G4NH<sub>2</sub> PAMAM dendrimers containing Ag and Au nanoparticles and were attributed to metal–dendrimer interactions [34].

Approximately four Pt–Pt coordination shells can be detected in the corresponding Fourier transforms of the raw EXAFS spectra collected with the freshly prepared Pt<sub>40</sub>-G4OH/ $\gamma$ -Al<sub>2</sub>O<sub>3</sub> sample, indicating the presence of Pt particles with relatively large

dimensions. For simplicity, only the first coordination shell of Pt was examined in detail and the best fit coordination parameters estimated from raw data for this shell are summarized in Table 2. The variances reported in Table 2 for both the imaginary and absolute parts are indicative of the high quality of the fit. Typically, when the variances are less than 1%, it is assumed that the model spectra closely fit the experimental data [35].

For the freshly prepared Pt<sub>40</sub>-G4OH/ $\gamma$ -Al<sub>2</sub>O<sub>3</sub> sample, the results of Table 2 indicate the presence of first-shell Pt–Pt contributions with an average coordination number of 7.3 at a bond distance of 2.77 Å. The average size of the Pt particles estimated from this average coordination number based on established correlations relating the average metal particle size to the first-shell metal–metal coordination number [36] is on the order of 1.4 nm. This value suggests that the Pt particles formed incorporate on average 42 metal atoms, with approximately 75% of those exposed on the surface of the metal particles. These EXAFS results are consistent with structural information reported previously for dendrimer-derived Pt/ $\gamma$ -Al<sub>2</sub>O<sub>3</sub> samples [7], where it was shown that the removal of the solvent and the configurational “collapse” of the dendrimer upon deposition on the support and drying lead to the formation of Pt nanoparticles.

STEM images (Fig. 2A) provide additional evidence for the Pt particle size in this sample. The particle size distribution obtained from such images is narrow, with the majority of Pt particles being in the size range of 0.4–1.6 nm and only a small fraction (i.e., 2.2%) in the 2.0–2.8 nm range (Fig. 2B). The surface-averaged size of Pt particles estimated from these data is approximately 1.6 nm, in good agreement with the value estimated from the EXAFS data.

The EXAFS data of Table 2 also show that the freshly prepared Pt<sub>40</sub>-G4OH/ $\gamma$ -Al<sub>2</sub>O<sub>3</sub> sample is characterized by a substantial amount of low-Z backscatterers (i.e., Pt–O(N) and Pt–C contributions), which are present in the first coordination shell of Pt at average distances of 2.03 and 2.16 Å, respectively. While it was established experimentally that backscattering amplitudes are not transferable between carbon and oxygen backscatterers, and therefore, these contributions can be separated in EXAFS spectra [37], the separation of oxygen and nitrogen neighbors is problematic [7]. As a result, no attempts were made to distinguish between Pt–O and Pt–N pairs. Considering the presence of the dendrimer, it is reasonable to assume that the Pt–C and Pt–O(N) contributions observed in the first coordination shell of Pt represent interactions between Pt and the functional groups of the dendrimer. Furthermore, it is also possible that a small fraction of Pt particles is in direct contact with the support surface, and therefore, some of the Pt–O(N) contributions could be attributed to Pt–support interactions. Consequently, the structural parameters reported in Table 2 for the Pt–O(N) contributions most likely represent a group of contributions arising from interactions of Pt particles with both the dendrimer molecules present on the support surface and the support itself, although the former are probably dominant.

The electronic state of Pt in the freshly prepared Pt<sub>40</sub>-G4OH/ $\gamma$ -Al<sub>2</sub>O<sub>3</sub> sample was examined by XPS. Since the most prominent Pt 4f signal overlaps with the Al 2p line [18,38,39], the Pt 4d region was used for the analysis. The XPS spectrum of the freshly prepared Pt<sub>40</sub>-G4OH/ $\gamma$ -Al<sub>2</sub>O<sub>3</sub> sample is shown in Fig. 3. The analysis of the second derivative of the raw data suggests the presence of two peaks in the spectrum, which can be assigned to the Pt 4d<sub>5/2</sub> and 4d<sub>3/2</sub> doublet. However, when a satisfactory fit was obtained with such an assumption, the FWHM values obtained for the Pt 4d doublet were on the order of 7.8 eV. This value is substantially larger than FWHM values typically reported in the literature for Pt 4d peaks [18], suggesting that the spectrum is more complex and likely incorporates signals from more than one Pt components. Therefore, the Pt 4d spectrum was further fitted to determine the minimum number of Pt components, with the constrain that the

**Table 1**  
Infrared bands characterizing selected characteristic vibrations of G4OH PAMAM dendrimer species in different samples.

Sample	Band position (cm <sup>-1</sup> )				Reference
	Amide I	Amide II	$\delta_{\text{CH}_2}$	Amide III	
G4OH film	1641	1556	1460	1362	[17]
G4OH/ $\gamma$ -Al <sub>2</sub> O <sub>3</sub>	1644	1557	1456	1371	[17]
Pt <sub>40</sub> -G4OH/ $\gamma$ -Al <sub>2</sub> O <sub>3</sub>	1641	1559	1457	1380	This work



**Table 2**  
Structural parameters characterizing Pt<sub>40</sub>-G4OH/ $\gamma$ -Al<sub>2</sub>O<sub>3</sub> samples after different treatments.<sup>a</sup>

Sample number	Treatment	Shell	N	R (Å)	10 <sup>3</sup> ·Δσ <sup>2</sup> (Å <sup>2</sup> )	ΔE <sub>0</sub> (eV)	k <sup>1</sup> -variances (%)	
							Im.	Abs.
1	Freshly prepared	Pt–Pt	7.3	2.77	0.00071	–3.4	0.15	0.07
		Pt–O(N)	0.9	2.03	0.00106	–1.7		
		Pt–C <sub>1</sub>	2.3	2.16	0.00176	–6.5		
		Pt–C <sub>2</sub>	0.9	3.11	–0.00580	5.2		
2	O <sub>2</sub> plasma at 25 °C for 60 min	Pt–Pt	6.8	2.77	0.00050	–5.1	0.36	0.16
		Pt–O(N) <sub>1</sub>	1.8	2.19	0.01000	–8.6		
		Pt–O(N) <sub>2</sub>	0.4	2.76	–0.00943	–2.6		
3	O <sub>2</sub> plasma at 25 °C for 90 min	Pt–Pt	6.9	2.77	0.00074	–5.1	0.24	0.11
		Pt–O(N) <sub>1</sub>	1.7	2.18	0.01000	–9.3		
		Pt–O(N) <sub>2</sub>	0.4	2.76	–0.00891	–3.3		
4	O <sub>2</sub> at 400 °C for 1 h	Pt–Pt	–	–	–	–	0.56	0.23
		Pt–O <sub>1</sub>	4.1	2.07	0.00680	0.7		
		Pt–O <sub>2</sub>	1.7	2.99	0.01000	1.5		
5	Sample #2 further treated in H <sub>2</sub> at 300 °C for 1 h	Pt–Pt	8.7	2.77	0.00043	–4.7	0.35	0.15
		Pt–O <sub>1</sub>	1.2	2.19	0.01000	–9.4		
		Pt–O <sub>2</sub>	0.4	2.76	–0.00860	–6.4		
6	Sample # 4 further treated in H <sub>2</sub> at 300 °C for 1 h	Pt–Pt	11.2	2.77	0.00626	0.7	0.48	0.24
		Pt–O <sub>1</sub>	0.8	2.17	0.01000	4.6		
		Pt–O <sub>2</sub>	0.3	2.80	–0.00963	5.0		

<sup>a</sup> Notation N, coordination number; R, distance between absorber and backscatterer atoms; Δσ<sup>2</sup>, change in the Debye–Waller factor value relative to the Debye–Waller factor of the reference compound; ΔE<sub>0</sub>, inner potential correction accounting for the difference in the inner potential between the sample and the reference compound. Estimated accuracies: N, ±20% (M–O, ±30%); R, ±1%; Δσ<sup>2</sup>, ±5%, ΔE<sub>0</sub>, ±10%.

FWHM values characterizing all the Pt 4d<sub>5/2</sub> and Pt 4d<sub>3/2</sub> lines should be in the 4.0–5.0 eV range and the split between the 4d<sub>5/2</sub> and 4d<sub>3/2</sub> lines should be approximately 17.0 eV for each Pt component, as reported elsewhere [18–21]. A good fit was obtained when two Pt components were included, as shown in Fig. 3. The binding energies for these peaks are reported in Table 3. The doublet at 314.1 and 331.0 eV can be assigned to the Pt 4d<sub>5/2</sub> and Pt 4d<sub>3/2</sub> lines, respectively, of fully reduced platinum species (Pt<sup>0</sup>) [38–41]. Furthermore, the second doublet with binding energies at 315.5 and 332.4 eV can be assigned to the Pt 4d<sub>5/2</sub> and Pt 4d<sub>3/2</sub> lines, respectively, of partially oxidized Pt<sup>δ+</sup> species, since the binding energies in this case are higher than those assigned to Pt<sup>0</sup> but lower than those typically observed for Pt<sup>2+</sup> species [38–41]. A comparison of the integral peak intensities for these two Pt components suggests that only 40% of the Pt species are fully reduced in the freshly prepared Pt<sub>40</sub>-G4OH/ $\gamma$ -Al<sub>2</sub>O<sub>3</sub> sample (Table 3). This result is consistent with previous literature reports also indicating incomplete reduction of Pt species coordinated to the dendrimer interior [7,10,42,43].

### 3.2. Effect of O<sub>2</sub> plasma treatment

Our previous FTIR and XPS data have shown that the dendrimer structure decomposes during O<sub>2</sub> plasma treatment at room temperature [17]. Measurements with thin G4OH PAMAM dendrimer films and with G4OH PAMAM dendrimers supported on  $\gamma$ -Al<sub>2</sub>O<sub>3</sub> have shown that in both cases, approximately 60 min were required to fragment the large majority of the dendrimer species. Therefore, a similar O<sub>2</sub> plasma treatment was applied to the Pt<sub>40</sub>-G4OH/ $\gamma$ -Al<sub>2</sub>O<sub>3</sub> sample in order to remove the dendrimer component and determine the effects of the O<sub>2</sub> plasma treatment on the structure and electronic state of the Pt particles.

The FTIR spectrum of a Pt<sub>40</sub>-G4OH/ $\gamma$ -Al<sub>2</sub>O<sub>3</sub> sample exposed to O<sub>2</sub> plasma at room temperature for 60 min is shown in Fig. 1 (spectrum 2). A comparison of this spectrum with the one collected for the freshly prepared Pt<sub>40</sub>-G4OH/ $\gamma$ -Al<sub>2</sub>O<sub>3</sub> sample (Fig. 1, spectrum 1) shows that the O<sub>2</sub> plasma treatment has destroyed the G4OH PAMAM dendrimer “signature”, since the characteristic bands as-

signed to the amide I (1641 cm<sup>−1</sup>), amide II (1559 cm<sup>−1</sup>),  $\delta_{\text{CH}_2}$  (1457 cm<sup>−1</sup>), and amide III (1380 cm<sup>−1</sup>) vibrations of the dendrimer structure are no longer observed in the spectrum of the plasma-treated sample.

Several new bands, however, were observed in the spectrum of the plasma-treated sample at 1700, 1640, 1593, 1403, and 1344 cm<sup>−1</sup>. The relatively broad band at 1640 cm<sup>−1</sup> can be assigned to the bending vibrations of water [32], which either remains in the sample after the impregnation step or is formed during the O<sub>2</sub> plasma treatment. In the case of the freshly prepared Pt<sub>40</sub>-G4OH/ $\gamma$ -Al<sub>2</sub>O<sub>3</sub> sample, this band overlaps with the strong amide I band and cannot be uniquely identified. However, the contribution of the bending vibrations of water becomes evident in the spectrum of the O<sub>2</sub> plasma-treated sample due to the absence of the amide I and amide II vibrations. The pair of bands with maxima at 1403 and 1344 cm<sup>−1</sup> can be assigned to water-solvated nitrate species coordinated to the  $\gamma$ -Al<sub>2</sub>O<sub>3</sub> surface. The split observed between these two bands is approximately 59 cm<sup>−1</sup>, consistent with the calculated value ( $\Delta\nu_3 = 58 \text{ cm}^{-1}$ ) reported in the literature for such species [44]. Identical results have been reported in the literature for  $\gamma$ -Al<sub>2</sub>O<sub>3</sub> exposed to vapors of HNO<sub>3</sub> and water [44].

Finally, two low-intensity bands at 1700 and 1593 cm<sup>−1</sup> appear as shoulders to the broad band at 1640 cm<sup>−1</sup> (Fig. 1, spectrum 2). The assignment of these bands is more ambiguous, since bands of different species (i.e., nitrates and carbonates) overlap significantly in this region. For example, the band at 1593 cm<sup>−1</sup> could be assigned to either bidentate nitrates or the  $\nu_{\text{CO}}$  vibration of bidentate carbonates [17,44–47], while the band at 1700 cm<sup>−1</sup> could be assigned to the bending mode of H<sub>3</sub>O<sup>+</sup> ions formed on the support or to the  $\nu_{\text{CO}}$  vibration of HCO<sub>3</sub><sup>−</sup> species [17,48,49]. The overall contribution of these two bands to the spectral intensity is relatively small, and at the end, the exact nature of the corresponding surface species may not be of a great importance. The more important point is that the dendrimer structure breaks down during the O<sub>2</sub> plasma treatment, and some of the decomposition products thus formed interact with the  $\gamma$ -Al<sub>2</sub>O<sub>3</sub> surface to form surface species of different nature, among which nitrates constitute a large fraction.

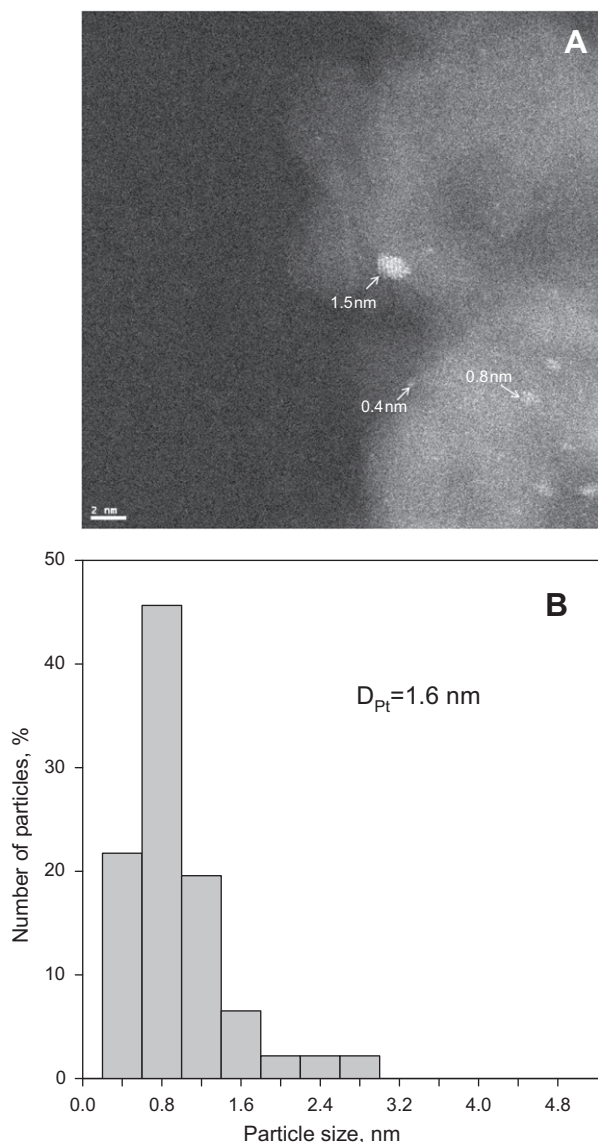


**Fig. 2.** STEM image (A) and corresponding particle size distribution (B) for a freshly prepared Pt<sub>40</sub>-G4OH/ $\gamma$ -Al<sub>2</sub>O<sub>3</sub> sample.

It was shown previously that the presence of Pt enhances the rate of dendrimer decomposition during treatments in the presence of O<sub>2</sub> at elevated temperatures [50]. A comparison of the FTIR data collected for Pt<sub>40</sub>-G4OH/ $\gamma$ -Al<sub>2</sub>O<sub>3</sub> with those reported previously for G4OH/ $\gamma$ -Al<sub>2</sub>O<sub>3</sub> samples [17] suggests that this is not the case for the O<sub>2</sub> plasma treatment, since a treatment time of approximately 60 min is required in both cases to decompose the majority of the dendrimer on the  $\gamma$ -Al<sub>2</sub>O<sub>3</sub> surface. Moreover, the same surface species are formed in both cases, and the presence of Pt does not affect their post-treatment concentrations on the  $\gamma$ -Al<sub>2</sub>O<sub>3</sub> support.

Subsequent treatment for the O<sub>2</sub> plasma-treated Pt<sub>40</sub>-G4OH/ $\gamma$ -Al<sub>2</sub>O<sub>3</sub> sample in H<sub>2</sub> at 300 °C for 1 h leads to significant changes in the FTIR spectrum (Fig. 1, spectrum 3). In particular, the intensities of all bands remaining in the spectrum (i.e., 1640, 1614, 1593, 1560, 1475, 1457, 1395, 1375, and 1316 cm<sup>-1</sup>) are significantly lower. These bands represent different forms of carbonates, since the majority of surface nitrates are removed from the  $\gamma$ -Al<sub>2</sub>O<sub>3</sub> surface during this treatment. This behavior is consistent with the lower thermal stability of surface nitrates and their ability to react

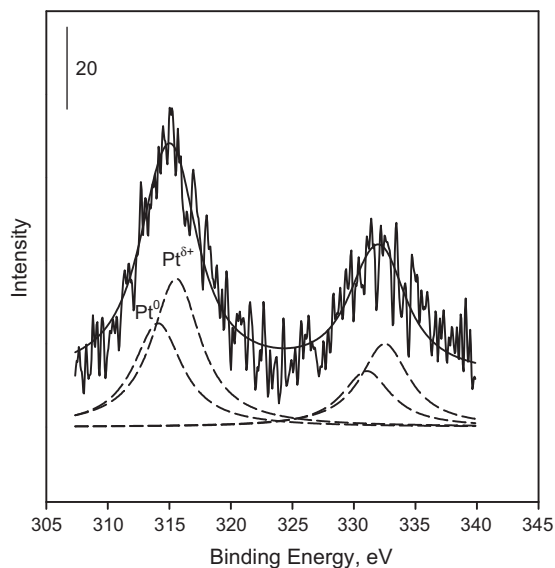


**Fig. 3.** XPS spectrum in the Pt 4d region of a freshly prepared Pt<sub>40</sub>-G4OH/ $\gamma$ -Al<sub>2</sub>O<sub>3</sub> sample (solid line) and corresponding fitting results (dotted line).

with H<sub>2</sub>, especially in the presence of noble metals, as reported elsewhere [49,51–53].

Pt particles with sizes ranging from 0.4 to 3.2 nm can be detected in the STEM images collected for the O<sub>2</sub> plasma-treated Pt<sub>40</sub>-G4OH/ $\gamma$ -Al<sub>2</sub>O<sub>3</sub> sample (Fig. 4A). The corresponding particle size distribution is relatively narrow with approximately 89% of the Pt particles being in the size range of 0.4–1.6 nm, while the rest are not larger than 3.2 nm (Fig. 4B). The surface-averaged size of the Pt particles estimated from these data is approximately 1.7 nm, which is essentially the same with the surface-averaged Pt particle size of the untreated sample (i.e., 1.6 nm). However, a comparison of the particle size distributions indicates a decrease in the fraction of particles in the 0.4–0.8 nm range, with a corresponding increase in the fraction of particles in the 1.2–1.6 nm range. These changes do not have a more significant effect on the average particle size calculated because of the small size of the particles affected. Overall, these results indicate that the O<sub>2</sub> plasma treatment has a minimal effect on the size of the Pt particles present.

The EXAFS data summarized in Table 2 further support such a conclusion. These data indicate that following exposure to O<sub>2</sub> plasma for 60 min, the Pt<sub>40</sub>-G4OH/ $\gamma$ -Al<sub>2</sub>O<sub>3</sub> sample is characterized by a first-shell Pt–Pt coordination number of 6.8 at a distance of 2.77 Å. An increase in the exposure time to 90 min does not affect the Pt–Pt contributions as both the first-shell Pt–Pt coordination number and the Pt–Pt bond distance remain essentially unchanged. A comparison of these results with those collected for the freshly prepared Pt<sub>40</sub>-G4OH/ $\gamma$ -Al<sub>2</sub>O<sub>3</sub> sample (Table 2) further suggests that the Pt particles remain essentially unchanged during the plasma treatment. One significant change, however, is the absence of any Pt–C contributions from the spectra of the plasma-treated samples. Such contributions were significant in the spectrum of the freshly prepared sample (Table 2) and were attributed to the interactions of Pt with the dendrimer structure in its vicinity. Their disappearance from the EXAFS spectrum is consistent with the FTIR results, indicating the decomposition of the dendrimer backbone during the O<sub>2</sub> plasma treatment.

XPS results obtained with the plasma-treated Pt<sub>40</sub>-G4OH/ $\gamma$ -Al<sub>2</sub>O<sub>3</sub> sample are shown in Table 3. The spectrum of this sample can be fitted with one Pt 4d<sub>5/2</sub> and Pt 4d<sub>3/2</sub> doublet with maxima located at binding energies of 315.5 and 332.4 eV, respectively,

**Table 3**  
XPS data characterizing Pt<sub>40</sub>-G4OH/ $\gamma$ -Al<sub>2</sub>O<sub>3</sub> samples after different treatments.

Sample number	Treatment	Pt4d <sub>5/2</sub> (eV)	Pt4d <sub>3/2</sub> (eV)	FWHM (eV)	Assigned species	Fraction of species (%)	Pt/Al atomic ratio ( $\times 10^{-3}$ )
1	Freshly prepared	314.1	331.0	4.8	Pt <sup>0</sup>	40	1.6
		315.5	332.4		Pt <sup><math>\delta</math>+</sup>	60	
2	O <sub>2</sub> plasma at 25 °C for 60 min	315.5	332.4	4.2	Pt <sup><math>\delta</math>+</sup>	100	1.5
3	O <sub>2</sub> at 400 °C for 1 h	316.0	332.9	4.3	Pt <sup>2+</sup>	100	1.1
4	Sample#2 further treated in H <sub>2</sub> at 300 °C for 1 h	314.2	331.3	4.7	Pt <sup>0</sup>	100	1.3
5	Sample#3 further treated in H <sub>2</sub> at 300 °C for 1 h	314.2	331.3	4.0	Pt <sup>0</sup>	100	0.9

indicating that Pt is present in a partially oxidized form (i.e., Pt <sup>$\delta$ +</sup>). This result is consistent with previous literature reports, indicating that metals undergo partial oxidation under O<sub>2</sub> plasma conditions. For example, when Au films deposited on silicon wafers were exposed to O<sub>2</sub> plasma, the formation of gold oxide species was observed at the surface layer of these films [54]. Similarly, XPS results reported elsewhere [55,56] indicate that surfaces of thin Pt films treated in O<sub>2</sub> plasma undergo partial oxidation. The same was found to be true for Pt nanoparticles supported on carbon [13]. Consistent with the STEM and EXAFS results, the XPS data also suggest that the dispersion of Pt was not affected significantly by the plasma treatment, since the surface Pt/Al atomic ratios are very similar for the freshly prepared and the plasma-treated Pt<sub>40</sub>-G4OH/ $\gamma$ -Al<sub>2</sub>O<sub>3</sub> samples (Table 3).

### 3.3. Effect of thermal treatment in O<sub>2</sub>

The frequently used alternative to the O<sub>2</sub> plasma treatment for the removal of the dendrimer component and the activation of the catalyst is a thermal treatment in O<sub>2</sub> [8–10]. As indicated in the past, temperatures of approximately 400 °C are needed in this case to successfully remove the dendrimer fragments from the catalyst surface [57]. The XPS spectrum of the Pt<sub>40</sub>-G4OH/ $\gamma$ -Al<sub>2</sub>O<sub>3</sub> sample treated in O<sub>2</sub> at 400 °C for 1 h consists of one doublet in the Pt 4d region with peak maxima at 316.0 and 332.9 eV, corresponding to 4d<sub>5/2</sub> and 4d<sub>3/2</sub> lines, respectively [19–21]. This result indicates that all Pt is oxidized to Pt<sup>2+</sup> following the thermal treatment in O<sub>2</sub> at 400 °C, in agreement with previous literature reports. For example, it has been shown that Pt particles smaller than 5 nm in diameter undergo complete oxidation following exposure to O<sub>2</sub> at elevated temperatures, while only the surface of Pt particles is oxidized when their size exceeds 5 nm [58]. EXAFS results reported previously for Pt/ $\gamma$ -Al<sub>2</sub>O<sub>3</sub> samples with Pt particles on the order of 1 nm are in agreement with this report, indicating the complete oxidative fragmentation of these small Pt particles in the presence of O<sub>2</sub> even at room temperature [59].

Consistent with these results, the EXAFS data reported in Table 2 for the thermally treated Pt<sub>40</sub>-G4OH/ $\gamma$ -Al<sub>2</sub>O<sub>3</sub> sample also indicate the fragmentation of the Pt particles, since no Pt–Pt contributions were found in the spectra. The EXAFS results further indicate that the thermal treatment in O<sub>2</sub> affects substantially the interaction of Pt with the  $\gamma$ -Al<sub>2</sub>O<sub>3</sub> support. More specifically, Pt–O<sub>support</sub> contributions, characterizing the bonding interactions of Pt atoms with oxygen atoms of the support, were observed in the plasma-treated sample at a distance of 2.19 Å, which is consistent with distances reported routinely for noble metal particles supported on various metal oxides [59,60]. In contrast, the same Pt–O<sub>support</sub> contributions in the thermally treated sample were observed at a much shorter distance (i.e., 2.07 Å), while at the same time, the coordination number was increased to 4.1 (Table 2). A comparison of these structural data with those reported elsewhere [61] for different Pt oxides suggests the complete conversion of the Pt metal particles to PtO species following the thermal treatment in O<sub>2</sub> at 400 °C,

since the first shell of Pt<sup>2+</sup> cations in PtO species consist of four oxygen atoms and the corresponding Pt–O distance is 2.06 Å [61].

Therefore, while it is evident from our previous reports that the dendrimer component can be effectively removed from the surface during thermal treatments in O<sub>2</sub> at 400 °C [57], both the XPS and EXAFS results described above clearly show that such thermal treatments render Pt oxide species rather than Pt metal particles on the surface of the  $\gamma$ -Al<sub>2</sub>O<sub>3</sub> support. STEM images (Fig. 5A) collected for the thermally treated Pt<sub>40</sub>-G4OH/ $\gamma$ -Al<sub>2</sub>O<sub>3</sub> sample show

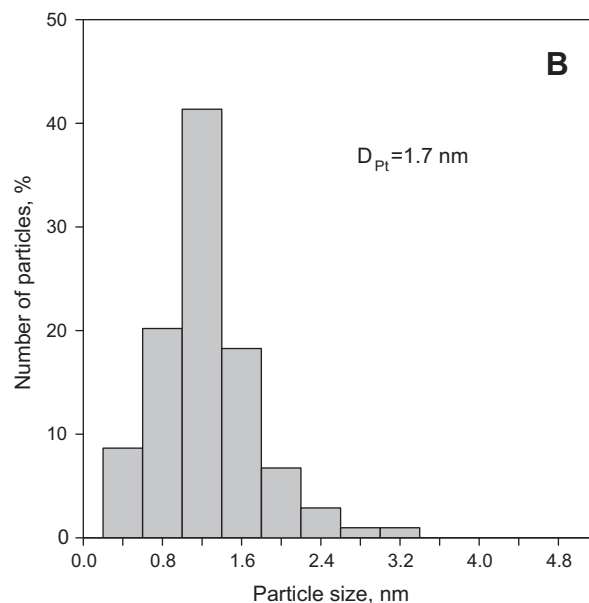
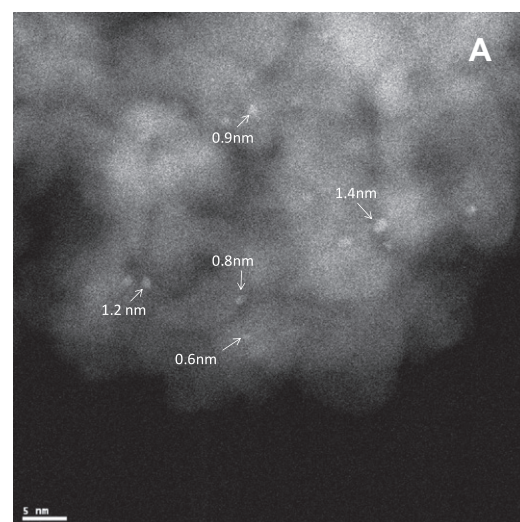


**Fig. 4.** STEM image (A) and corresponding particle size distribution (B) for a Pt<sub>40</sub>-G4OH/ $\gamma$ -Al<sub>2</sub>O<sub>3</sub> sample treated in O<sub>2</sub> plasma at room temperature for 1 h.



that the platinum oxide particles thus formed are not uniform in size, ranging from 1.2 to 5.2 nm. The corresponding particle size distribution (Fig. 5B) is bimodal, with approximately 79% of the PtO particles being in the size range of 1.2–3.2 nm and the remaining 21% having sizes in the 3.6–5.2 nm range. A comparison of this particle size distribution with that shown in Fig. 2 for the freshly prepared sample clearly shows that substantial sintering of the Pt species takes place during the O<sub>2</sub> treatment at 400 °C. As a result, the average size of the PtO particles in the thermally treated sample was found to be 3.5 nm, which is 2.2 times greater than the average particle size for the freshly prepared sample. The XPS results reported in Table 3 further confirm the sintering of Pt, since the surface Pt/Al atomic ratio estimated for the thermally treated Pt<sub>40</sub>-G4OH/ $\gamma$ -Al<sub>2</sub>O<sub>3</sub> sample was found to be approximately 30% smaller than the corresponding ratio determined for the freshly prepared and the plasma-treated samples.

### 3.4. Effect of thermal treatment in H<sub>2</sub>

When Pt<sub>40</sub>-G4OH/ $\gamma$ -Al<sub>2</sub>O<sub>3</sub> samples thermally treated in O<sub>2</sub> at 400 °C or treated in O<sub>2</sub> plasma at room temperature were exposed

to H<sub>2</sub> at 300 °C for 2 h, a single set of Pt 4d<sub>5/2</sub> and Pt 4d<sub>3/2</sub> peaks with binding energies of 314.2 and 331.3 eV (Table 3), respectively, was observed in their XPS spectra, indicating the presence of only completely reduced Pt. Therefore, both the Pt<sup>δ+</sup> and the Pt<sup>2+</sup> species, which were previously observed depending on the O<sub>2</sub> treatment used, were completely converted into metallic Pt species during the H<sub>2</sub> treatment at 300 °C. This result is not surprising since it has been shown previously that highly dispersed PtO species can be completely converted to metallic platinum clusters during exposure to H<sub>2</sub> even at room temperature [59].

Analysis of STEM images of the sample treated first in O<sub>2</sub> plasma and then in H<sub>2</sub> (Fig. 6A) indicates the presence of Pt particles with sizes in the 0.8–3.6 nm range. The corresponding particle size distribution is still relatively narrow (Fig. 6B), yielding an average Pt particle size of 2 nm. This average size is only slightly larger than the 1.6 nm value obtained for the freshly prepared sample, indicating that the combination of a room temperature O<sub>2</sub> plasma treatment and a high temperature H<sub>2</sub> treatment can be used to remove the dendrimer component from the Pt<sub>40</sub>G4OH/ $\gamma$ -Al<sub>2</sub>O<sub>3</sub> sample with minimal sintering of the Pt particles.

EXAFS data collected for this sample (Table 2) further confirm this conclusion. More specifically, when the plasma-treated sample was exposed to H<sub>2</sub> at 300 °C for 2 h, the first-shell Pt–Pt coordination number increased from 6.8 to 8.7, while the Pt–Pt distance remained the same. At the same time, the number of oxygen atoms adjacent to Pt at a bonding distance of 2.19 Å decreased (Table 2), indicating a decreased contribution from the Pt–support interface, consistent with an increase in Pt particle size. Moreover, the 8.7 value for the first-shell Pt–Pt coordination number corresponds to the formation of Pt particles with average dimensions on the order of 2.1 nm [36], in agreement with the 2 nm average particle size estimated from the STEM data. A similar trend is also observed in Pt/Al atomic ratios obtained from the XPS data (Table 3).

A much higher degree of sintering was observed when the combination of two thermal treatments in O<sub>2</sub> and H<sub>2</sub> was used for the dendrimer removal. We reported previously that dendrimer-derived Pt/ $\gamma$ -Al<sub>2</sub>O<sub>3</sub> samples exposed to thermal O<sub>2</sub>/H<sub>2</sub> treatments show an increase in the Pt particle sizes from 1 to 4 nm [7]. This severe sintering of Pt was attributed to the high mobility of Pt nanoparticles on the dendrimer surface during the initial stages of dendrimer removal at elevated temperatures [7]. The more recent results described in this paper confirm the degree of sintering but also show that the process is more complex, since the treatment in O<sub>2</sub> at 400 °C not only removes the dendrimer component but also converts the Pt nanoparticles into Pt oxide species, which in turn aggregate on the support surface. Since previous literature reports indicate that highly dispersed Pt particles can be converted into Pt oxide during O<sub>2</sub> treatments even at room temperature [59], it is possible that the rate of Pt oxidation exceeds substantially the rate of the dendrimer decomposition process. Thus, it is also possible that initially formed Pt oxide species are mostly interacting with the dendrimer surface rather than the support and, therefore, could have a much higher mobility than similar species formed on the surface of  $\gamma$ -Al<sub>2</sub>O<sub>3</sub>.

Regardless of the reasons, the sintering of Pt oxide species appears to be the main contributor to the overall Pt aggregation, since the effect of the subsequent H<sub>2</sub> treatment on the Pt particle size is relatively small and similar to that observed for the case of the plasma-treated sample. More specifically, an average Pt particle size of 3.9 nm was obtained from the STEM data for the thermally treated sample following the reduction at 300 °C. Similarly, the first-shell Pt–Pt coordination number increased to 11.2 for this sample (Table 2), indicating a Pt particle size on the order of 4 nm. This size is only slightly larger than the size of the Pt oxide species (3.5 nm) formed after the thermal O<sub>2</sub> treatment step. Therefore, the treatment in H<sub>2</sub> at 300 °C increases the size of the

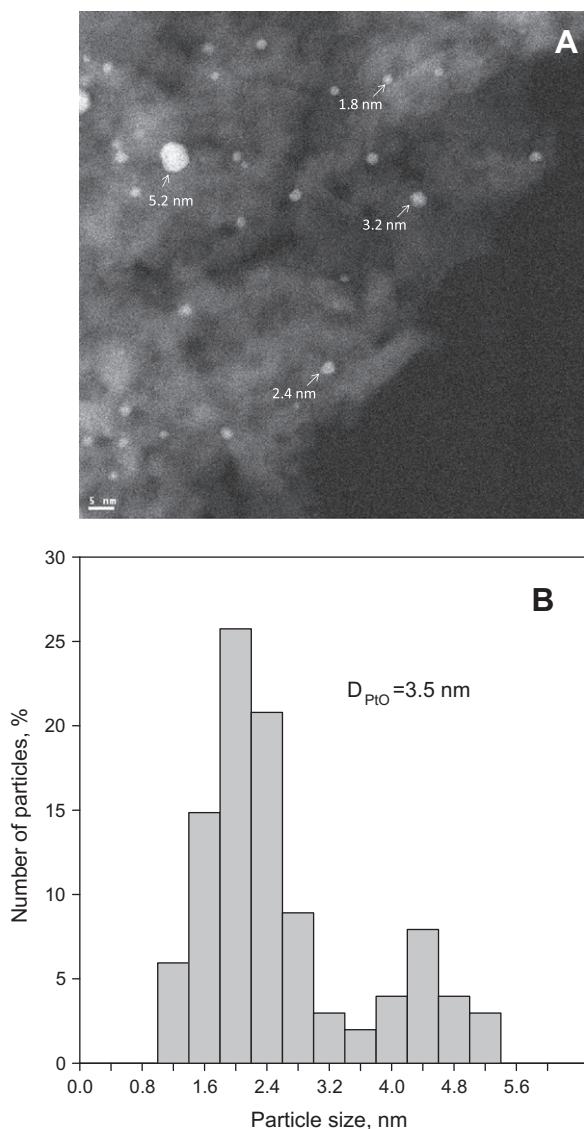


**Fig. 5.** STEM image (A) and corresponding particle size distribution (B) for a Pt<sub>40</sub>-G4OH/ $\gamma$ -Al<sub>2</sub>O<sub>3</sub> sample treated in O<sub>2</sub> at 400 °C for 1 h.



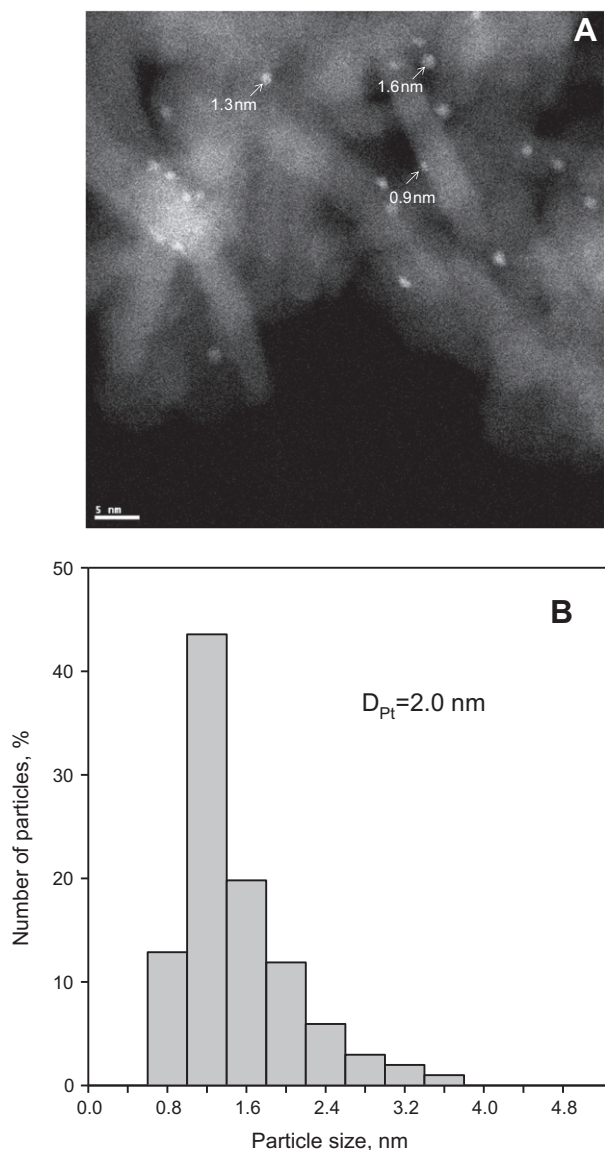


**Fig. 6.** STEM image (A) and corresponding particle size distribution (B) for a  $\text{Pt}_{40}\text{-G4OH}/\gamma\text{-Al}_2\text{O}_3$  sample treated first at room temperature in  $\text{O}_2$  plasma for 1 h and then in  $\text{H}_2$  at  $300^\circ\text{C}$  for 1 h.

Pt particles by 10–15%, which is comparable with what was observed in the case of plasma-treated sample.

Finally, chemisorption data characterizing  $\text{Pt}_{40}\text{-G4OH}/\gamma\text{-Al}_2\text{O}_3$  samples which were either plasma- or thermally treated and subsequently exposed to  $\text{H}_2$  at  $300^\circ\text{C}$  are summarized in Table 4. In each case, the H/Pt and O/Pt ratios were found to be in a good agreement with each other. The average diameters of Pt particles estimated from these chemisorption data are in excellent agreement with those obtained from the STEM and EXAFS measurements (Table 4), providing further support for the conclusion

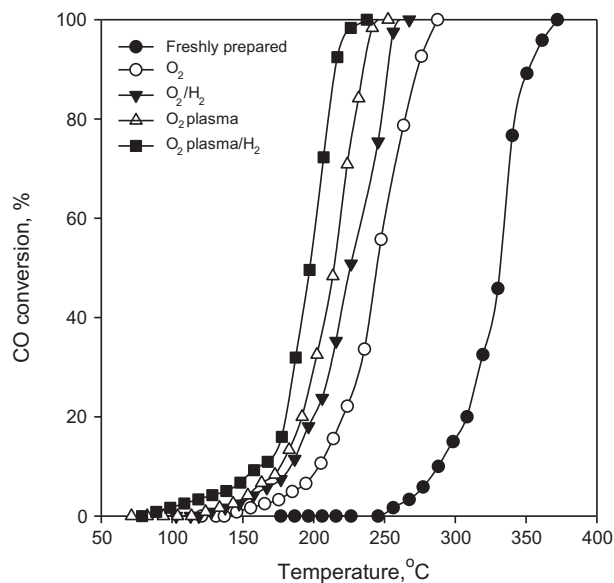


**Fig. 7.** CO conversions observed during the oxidation of CO over different  $\text{Pt}_{40}\text{-G4OH}/\gamma\text{-Al}_2\text{O}_3$  samples: (●) freshly prepared; (○) treated in  $\text{O}_2$  at  $400^\circ\text{C}$  for 1 h; (▼) treated first in  $\text{O}_2$  at  $400^\circ\text{C}$  for 1 h and then in  $\text{H}_2$  at  $300^\circ\text{C}$  for 1 h; (△) treated in  $\text{O}_2$  plasma at  $25^\circ\text{C}$  for 1 h; (■) treated first in  $\text{O}_2$  plasma at  $25^\circ\text{C}$  for 1 h and then in  $\text{H}_2$  at  $300^\circ\text{C}$  for 1 h (reaction conditions: 1000 ppm CO, 500 ppm  $\text{O}_2$ , balance He, GHSV = 100,000  $\text{ml}/(\text{g}_{\text{cat}} \text{ h})$ ).

that the  $\text{O}_2$  plasma treatment does not significantly affect the dispersion of the Pt species.

### 3.5. Catalytic properties of $\text{Pt}_{40}\text{-G4OH}/\gamma\text{-Al}_2\text{O}_3$ catalysts

#### 3.5.1. CO oxidation

Fig. 7 shows the CO conversions obtained at various reaction temperatures over  $\text{Pt}_{40}\text{-G4OH}/\gamma\text{-Al}_2\text{O}_3$  samples exposed to different treatments. With the freshly prepared sample, a measurable conversion of CO was observed only at temperatures above  $250^\circ\text{C}$  and a temperature of  $370^\circ\text{C}$  was required to achieve full conversion of CO under the conditions examined. The absence of any catalytic activity at temperatures below  $250^\circ\text{C}$  indicates that the Pt particles initially present in this sample are “shielded” by the dendrimer component and, therefore, are inaccessible to the reactants. This model is consistent with FTIR data reported in the literature and indicating the absence of any CO adsorption on  $\text{Pt}_{40}\text{-G4OH}/\text{SiO}_2$  materials prior to any thermal treatment [57]. TGA data reported elsewhere [62] for Pt-G4OH films show that a large fraction of the dendrimer component decomposes in the  $200\text{--}300^\circ\text{C}$  temperature range. Therefore, the appearance of the CO oxidation activity within this temperature range is consistent with the Pt particles becoming accessible to the reactants following the in situ dendrimer decomposition and subsequent removal.

The CO light-off curve for the sample thermally activated in  $\text{O}_2$  at  $400^\circ\text{C}$  is shifted to the low temperature region by

**Table 4**

Sizes of metal particles and TOF values for CO oxidation and  $\text{C}_2\text{H}_6$  hydrogenolysis over  $\text{Pt}_{40}\text{-G4OH}/\gamma\text{-Al}_2\text{O}_3$  samples following different treatments.

Treatment	O/Pt ratio	H/Pt ratio	Pt particle size, nm			TOF ( $\text{s}^{-1}$ )	
			EXAFS	STEM	Chemisorption	CO oxidation at $140^\circ\text{C}$	$\text{C}_2\text{H}_6$ hydrogenolysis at $325^\circ\text{C}$
$\text{O}_2$ at $400^\circ\text{C}$ for 1 h followed by $\text{H}_2$ at $300^\circ\text{C}$ for 1 h	0.29	0.27	4.0	3.9	4.0	$5.3 \times 10^{-3}$	$3.7 \times 10^{-2}$
$\text{O}_2$ plasma at room temperature for 1 h followed by $\text{H}_2$ at $300^\circ\text{C}$ for 1 h	0.56	0.52	2.1	2.0	2.1	$5.4 \times 10^{-3}$	$6.3 \times 10^{-2}$

approximately 85 °C, while the shift is even larger (i.e., 110 °C) in the case of the plasma-treated sample. In addition to differences in Pt dispersion, differences in the oxidation state of Pt may also be contributing to the differences observed in the performance of these samples. More specifically, the EXAFS and XPS results described above indicate that the thermal treatment in O<sub>2</sub> leads to the formation of Pt oxide species (Pt<sup>2+</sup>), while Pt particles with a partial cationic character (i.e., Pt<sup>δ+</sup>) are present in the plasma-treated sample. The latter are expected to be more active in CO oxidation because such species bind CO less strongly than fully oxidized Pt<sup>2+</sup> species [63].

Regardless of the O<sub>2</sub> treatment used to remove the dendrimer component, the XPS and EXAFS results further show that the subsequent treatment in H<sub>2</sub> results in the formation of Pt particles, which are metallic in nature. The catalytic data (Fig. 7) also show that the reduction treatment results in a further shift of the light-off curves to lower temperatures by approximately 20 °C in both cases. Once again, this shift implies that the oxidation state of Pt is an important factor in CO oxidation with the reduced metal species being more active than the oxidized ones. Furthermore, the difference observed between the two reduced samples can no longer be attributed to the oxidation state of Pt but rather can be explained by differences in the Pt dispersion. Indeed, a comparison of the turnover frequency (TOF) values calculated for these samples at 140 °C (to ensure that the reaction proceeds under differential conditions) supports such a conclusion, since nearly the same TOF value was obtained for both samples (Table 4). Therefore, the differences observed between the light-off curves can be attributed to the higher number of surface Pt sites present in the plasma-treated sample due to the lower average Pt particle size. Furthermore, the similar TOF values obtained despite the difference in particle size are consistent with the structure-insensitive nature of the CO oxidation reaction [64,65].

Finally, the TOF values obtained are lower than those reported in the literature for conventionally prepared catalyst of the same composition. More specifically, turnover frequencies on the order of  $3 \times 10^{-2} \text{ s}^{-1}$  and  $9 \times 10^{-2} \text{ s}^{-1}$  have been reported for the oxidation of CO over Pt/ $\gamma$ -Al<sub>2</sub>O<sub>3</sub> when the reaction was performed at 130 and 150 °C, respectively [65,66]. These values are approximately one order of magnitude larger than what was observed in our case. However, in these literature examples, much higher concentrations of oxygen were used in the reaction feed (i.e., 10–20%), as compared to 500 ppm in our case. Therefore, given the dependence of the CO oxidation rate on O<sub>2</sub> pressure [65], the observed difference in turnover frequencies should be at least in part attributed to the differences in feed compositions used.

### 3.5.2. C<sub>2</sub>H<sub>6</sub> hydrogenolysis

The hydrogenolysis of ethane is a structure-sensitive reaction, for which smaller Pt particles exhibit higher TOF values. For example, it has been reported that the turnover frequencies for this reaction over supported Pt decreases approximately 1.6 times as the Pt particle size increases from 1.7 to 3.6 nm [67]. Detailed mechanistic investigations have attributed this behavior to the increased fraction of low coordination highly energetic Pt sites in the smaller particles [68–71]. Consistent with these trends, the kinetic results obtained for the Pt<sub>40</sub>-G4OH/ $\gamma$ -Al<sub>2</sub>O<sub>3</sub> samples exposed to the plasma and thermal treatments clearly show a higher TOF value for samples subjected to the former treatment (Table 4). In fact, the initial TOF values reported in Table 4 for 2 and 4 nm Pt particles vary by a factor of 1.7, and this difference is consistent with that reported previously in the literature for Pt particles of similar sizes [67]. Furthermore, the TOF values for the dendrimer-derived samples fall within the wide range of TOF values (i.e.,  $1 \times 10^{-3}$ – $2.4 \times 10^{-1} \text{ s}^{-1}$ ) reported previously in the literature by different groups for the hydrogenolysis of ethane over supported Pt particles

with sizes ranging between 1.3 and 7 nm [67,72–76]. A more precise comparison of TOF values is not possible at this point because of the significant differences in the experimental conditions used in these reports. The apparent activation energy values were found to be similar after both treatments (i.e., approximately 36 kcal/mol), once again, consistent with the 23–65 kcal/mol range reported previously for supported Pt catalysts with metal particle sizes in the 1–7 nm range [67,72–77]. Overall, these catalytic results provide further unambiguous evidence that the O<sub>2</sub> plasma treatment effectively removes the dendrimer component and renders catalytically active Pt particles on the support surface without a significant effect on the metal dispersion.

## 4. Conclusions

A room temperature O<sub>2</sub> plasma treatment was used to activate dendrimer-derived Pt<sub>40</sub>-G4OH/ $\gamma$ -Al<sub>2</sub>O<sub>3</sub> materials by removing the dendrimer component from the surface. FTIR results show that such a plasma treatment decomposes the dendrimer component, since its spectroscopic “signature” completely disappears from the spectra after approximately 60 min of treatment. The presence of Pt in the sample does not change the dendrimer decomposition rate under O<sub>2</sub> plasma conditions. Inability of the O<sub>2</sub> plasma to break up Pt–Pt bonds (as confirmed by EXAFS) is a key feature and the main advantage of this treatment. As a result, the average size of Pt particles remains nearly unchanged after the plasma treatment. A subsequent treatment in H<sub>2</sub> at 300 °C leads to some aggregation of Pt, but the degree of such aggregation is small and the average Pt particle size remains below 2 nm. In contrast, when a conventional thermal treatment in O<sub>2</sub> at 400 °C was used to remove the dendrimer component, the Pt particles were completely converted into PtO species, which further aggregated on the surface yielding an average particle size on the order of 3.5 nm. Subsequent treatment in H<sub>2</sub> at 300 °C resulted in the formation of 4 nm Pt particles. Overall, the combination of the high temperature O<sub>2</sub>/H<sub>2</sub> treatments leads to the severe sintering of Pt particles, with the major sintering step taking place during the oxidation process. Catalytic results for the oxidation of CO and the hydrogenolysis of ethane further demonstrate the differences between samples having different sizes of Pt particles as a result of the different treatments used for the removal of the dendrimer component. Since the dendrimer-derived catalysts activated in O<sub>2</sub> plasma exhibit very narrow particle size distributions, they provide a unique opportunity for examining structure-sensitivity effects for a large number of reactions catalyzed by Pt and other noble metals.

## Acknowledgments

The authors gratefully acknowledge Toyota Motor Engineering & Manufacturing North America, Inc., for the partial financial support of this work, as well as permission to publish the results. The authors further acknowledge Dr. Douglas Blom at the Electron Microscopy Center of the University of South Carolina for his assistance during the collection of the STEM images.

## Appendix A. Supplementary material

Supplementary data associated with this article can be found, in the online version, at <http://dx.doi.org/10.1016/j.jcat.2012.02.016>.

## References

- [1] D. Astruc (Ed.), *Nanoparticles and Catalysis*, Wiley, Weinheim, 2008.
- [2] C.-J. Jia, F. Schüth, *Phys. Chem. Chem. Phys.* 13 (2011) 2457.
- [3] A. Roucoux, J. Schulz, H. Patin, *Chem. Rev.* 102 (2002) 3757.
- [4] C. Burda, X. Chen, R. Narayanan, M.A. El-Sayed, *Chem. Rev.* 105 (2005) 1025.

- [5] R. Andrés, E. Jesús, J.C. Flores, *New J. Chem.* 31 (2007) 1161.
- [6] K. Kimura, H. Einaga, Y. Teraoka, *Catal. Lett.* 139 (2010) 72.
- [7] O.S. Alexeev, A. Siani, G. Lafaye, C.T. Williams, H.J. Ploehn, M.D. Amiridis, *J. Phys. Chem. B* 110 (2006) 24903.
- [8] A. Siani, O.S. Alexeev, D.S. Deutsch, J.R. Monnier, P.T. Fanson, H. Hirata, S. Matsumoto, C.T. Williams, M.D. Amiridis, *J. Catal.* 266 (2009) 331.
- [9] G. Lafaye, A. Siani, P.G. Marécot, M.D. Amiridis, C.T. Williams, *Phys. Chem. B* 110 (2006) 7725.
- [10] W. Hung, J.N. Kuhn, C. Tsung, Y. Zahng, S.E. Habas, P. Yang, G.A. Somorjai, *Nano Lett.* 8 (2008) 2027.
- [11] C. Lee, H.W. Kim, S. Kim, *Appl. Surf. Sci.* 253 (2007) 3658.
- [12] U. Cvelbar, S. Pejovnik, M. Mozetie, A. Zalar, *Appl. Surf. Sci.* 210 (2003) 255.
- [13] Y.E. Seidel, R. Lindström, Z. Jusys, J. Cai, U. Wiedwald, P. Ziemann, R.J. Behm, *Langmuir* 23 (2007) 5795.
- [14] S. Kiehlbass, A. Häbich, J. Schnaidt, J. Bannmann, F. Weigl, H.-G. Boyen, P. Ziemann, R.J. Behm, *Langmuir* 22 (2006) 7873.
- [15] D.-G. Cheng, *Catal. Surv. Asia* 12 (2008) 145.
- [16] J. Zheng, R. Yang, L. Xie, J. Qu, Y. Liu, X. Li, *Adv. Mater.* 22 (2010) 1451.
- [17] Z. Nazarpoor, S. Ma, P.T. Fanson, O.S. Alexeev, M.D. Amiridis, *Polym. Degrad. Stabil.* 97 (2012) 439.
- [18] A.V. Kalinkin, M.Yu. Smirnov, A.I. Nizovskii, V.I. Bukhtiyarov, *J. Electron Spectrosc.* 177 (2010) 15.
- [19] L. Olsson, E. Fridé, *J. Catal.* 210 (2002) 340.
- [20] Z. Zsoldos, L. Gucci, *J. Phys. Chem.* 96 (1992) 9393.
- [21] J.Z. Shyu, K. Otto, *Appl. Surf. Sci.* 32 (1988) 246.
- [22] R.E. Jentoft, S.E. Deutsch, B.C. Gates, *Rev. Sci. Instrum.* 67 (1996) 2111.
- [23] M. Vaarkamp, J.C. Linders, D.C. Koningsberger, *Physica B* 208–209 (1995) 159.
- [24] D.C. Koningsberger, in: C.A. Melendres, A. Tadjeddine (Eds.), *Synchrotron Techniques in Interfacial Electrochemistry*, Kluwer, Dordrecht, 1994.
- [25] P.S. Kirlin, F.B.M. Van Zon, D.C. Koningsberger, B.C. Gates, *J. Phys. Chem.* 94 (1990) 8439.
- [26] J.B.A.D. Van Zon, D.C. Koningsberger, H.F.J. Van't Blik, D.E. Sayers, *J. Chem. Phys.* 82 (1985) 5742.
- [27] B.K. Teo, P.A. Lee, *J. Am. Chem. Soc.* 101 (1979) 2815.
- [28] F.B.M. Duivenvoorden, D.C. Koningsberger, Y.S. Uh, B.C. Gates, *J. Am. Chem. Soc.* 108 (1986) 6254.
- [29] A. Siani, O.S. Alexeev, B. Captain, G. Lafaye, P. Marécot, R.D. Adams, M.D. Amiridis, *J. Catal.* 255 (2008) 162.
- [30] E.A. Stern, *Phys. Rev. B* 48 (1993) 9825.
- [31] E.O. Bringham, *The Fast Fourier Transform*, Prentice Hall, Englewood Cliffs, NJ, 1974.
- [32] J.-B. Brubach, A. Mermet, A. Filabozzi, A. Gerschel, P. Ray, *J. Chem. Phys.* 122 (2005) 184509.
- [33] F. Tarazona-Vasquez, P.B. Balbuena, *J. Phys. Chem. B* 108 (2004) 15982.
- [34] A. Manna, T. Imae, K. Aoi, M. Okada, T. Yogo, *Chem. Mater.* 13 (2001) 1674.
- [35] D.C. Koningsberger, B.L. Mojet, G.E. van Dorssen, D.E. Ramaker, *Top. Catal.* 10 (2000) 143.
- [36] B.J. Kip, F.B.M. Duivenvoorden, D.C. Koningsberger, R. Prins, *J. Catal.* 105 (1987) 26.
- [37] K.I. Pandya, D.C. Koningsberger, *Physica B* 158 (1989) 386.
- [38] A. Mihaylova, A. Tsanev, P. Stefanov, D. Stoychev, T. Marinova, *React. Kinet. Catal. Lett.* 84 (2005) 121.
- [39] B. Riguette, S. Damyanova, G. Goluliev, C. Marques, L. Petrov, J.M. Bueno, *J. Phys. Chem. B* 108 (2004) 5349.
- [40] J.C. Serrano-Ruiz, G.W. Huber, M.A. Sánchez-Castillo, J.A. Dumesic, F. Rodríguez-Reinoso, A. Sepúlveda-Escribano, *J. Catal.* 241 (2006) 378.
- [41] T. Ruhle, H. Schneider, J. Find, D. Herein, N. Pfander, U. Wild, R. Schlogl, D. Nachtingall, S. Artelt, U. Heinrich, *Appl. Catal. B* 14 (1997) 69.
- [42] Y. Borodko, C.M. Thompson, W. Huang, H.B. Yildiz, H. Frei, G.A. Somorjai, *J. Phys. Chem. C* 115 (2011) 4757.
- [43] M.R. Knecht, M.G. Weir, V.S. Myers, W.D. Pyrz, H. Ye, P. Valeri, D.J. Buttrey, A.I. Frenkel, R.M. Crooks, *Chem. Mater.* 20 (2008) 5218.
- [44] J. Baltrusaitis, J. Schuttlefield, J.H. Jensen, V.H. Grassian, *Phys. Chem. Chem. Phys.* 9 (2007) 4970.
- [45] M.A. Zondlo, S.B. Barone, M.A. Tolbert, *Geophys. Res. Lett.* 24 (1997) 1391.
- [46] C.D. Mashburn, E.K. Frinak, M.A.J. Tolbert, *Geophys. Res. Lett.* 111 (2006) 10.
- [47] K. Fottinger, R. Schlogl, G. Rupprechter, *Chem. Commun.* (2008) 320.
- [48] A. Iordan, M.I. Zaki, C. Kappenstein, *Phys. Chem. Chem. Phys.* 6 (2004) 2502.
- [49] M.I. Baraton, X. Chen, K.E. Gonsalves, *Nanostruct. Mater.* 8 (1997) 435.
- [50] S.D. Deutsch, A. Siani, P.T. Fanson, H. Hirata, S. Matsumoto, C.T. Williams, M.D. Amiridis, *J. Phys. Chem. C* 111 (2007) 4246.
- [51] F. Peinotto, G. Ghiotti, I. Nova, L. Lietti, E. Tronconi, P. Forzatti, *J. Phys. Chem. B* 105 (2001) 12732.
- [52] C.B. Wang, T.F. Yeh, H.K. Lin, *J. Hazard. Mater.* B92 (2002) 241.
- [53] N.W. Cant, M.J. Patterson, *Catal. Lett.* 85 (2003) 153.
- [54] K. Raiber, A. Terfort, C. Benndorf, N. Krings, H.H. Strehblow, *Surf. Sci.* 595 (2005) 56.
- [55] J.J. Blackstock, D.R. Stewart, Z. Li, *Appl. Phys. A* 80 (2005) 1343.
- [56] Z. Li, P. Beck, D.A.A. Ohlberg, D.R. Stewart, R.S. Williams, *Surf. Sci.* 529 (2003) 410.
- [57] S.D. Deutsch, G. Lafaye, D. Liu, B.D. Chandler, C.T. Williams, M.D. Amiridis, *Catal. Lett.* 97 (2004) 139.
- [58] R.K. Herz, E.J. Shinouskis, *Appl. Surf. Sci.* 19 (1984) 373.
- [59] O.S. Alexeev, F. Li, M.D. Amiridis, B.C. Gates, *J. Phys. Chem. B* 109 (2005) 2338.
- [60] O.S. Alexeev, B.C. Gates, *Ind. Eng. Chem. Res.* 42 (2003) 1571.
- [61] N. Seriani, Z. Jin, W. Pompe, L. Ciacchi, *Phys. Rev. B* 76 (2007) 155421.
- [62] O. Ozturk, T.J. Black, K. Perrine, K. Pizzolato, C.T. Williams, F.W. Parsons, J.S. Ratliff, J. Gao, C.J. Murphy, H. Xie, H.J. Ploehn, D.A. Chen, *Langmuir* 21 (2005) 3998.
- [63] O.S. Alexeev, S.Y. Chin, M.H. Engelhard, L. Ortiz-Soto, M.D. Amiridis, *J. Phys. Chem. B* 109 (2005) 23430.
- [64] M. Boudart, F. Rumpf, *React. Kinet. Catal. Lett.* 35 (1987) 95.
- [65] A.D. Allian, K. Takanabe, K.L. Fajdala, X. Hao, T.J. Truex, J. Cai, C. Buda, M. Neurock, E. Iglesia, *J. Am. Chem. Soc.* 133 (2011) 4498.
- [66] L. Liu, F. Zhou, L. Wang, X. Qi, F. Shi, Y. Deng, *J. Catal.* 274 (2010) 1.
- [67] R.M. Rioux, H. Song, J.D. Hoefelmeyer, P. Yang, G.A. Somorjai, *J. Phys. Chem. B* 109 (2005) 2192.
- [68] J.H. Sinfelt, D.J.C. Yates, *J. Catal.* 8 (1967) 82.
- [69] J.H. Sinfelt, *Catal. Rev.* 3 (1970) 175.
- [70] H. Song, R.M. Rioux, J.D. Hoefelmeyer, R. Komor, K. Niesz, M. Grass, P. Yang, G.A. Somorjai, *J. Am. Chem. Soc.* 128 (2006) 3027.
- [71] G.A. Somorjai, J. Park, *Top. Catal.* 49 (2008) 126.
- [72] H. Cho, S.B. Park, S.J. Cho, R. Ryoo, *J. Catal.* 173 (1998) 295.
- [73] D. Nazimek, J. Ryczkowski, *React. Kinet. Catal. Lett.* 40 (1989) 145.
- [74] J.H. Sinfelt, *J. Phys. Chem.* 68 (1964) 344.
- [75] R.D. Cortright, R.M. Watwe, B.E. Spiewak, J.A. Dumesic, *Catal. Today* 53 (1999) 395.
- [76] J.H. Sinfelt, W.F. Taylor, D.J.C. Yates, *J. Phys. Chem.* 69 (1965) 95.
- [77] B.S. Gudkov, G. Gucci, P. Tétényi, *J. Catal.* 74 (1982) 207.